Supporting Information

Schotte et al. 10.1073/pnas.1210938109

SI Materials and Methods

Interpolated Ratio Method. The diffraction spots in each image of a time series were indexed and integrated, and the crystal orientation refined. The structural information we seek is encoded in pump-induced changes of the spot intensities, whose absolute amplitude depends on crystal volume, crystal orientation, the X-ray wavelength exciting the corresponding Bragg reflections, and the X-ray intensity. To minimize systematic sources of error that can arise when merging diffraction data acquired at different orientations on different crystals, we use a variation of the ratio method developed by Coppens et al. (1) and Vorontsov et al. (2). That method is based upon back-to-back diffraction images acquired with (ON) and without (OFF) a laser pump pulse. By merging I_{ON}/I_{OFF} ratios of integrated spot intensities for each indexed reflection (R_{hkl}), instead of intensity differences (ΔI_{hkl}), errors arising from image scaling and wavelength normalization are avoided. After merging, the ratios can be converted to structure factor amplitude differences by multiplying each ground-state structure factor amplitude by its corresponding $R_{hkl} - 1$.

Instead of using I_{ON}/I_{OFF}, we use I_{ON}/I_{REF} where I_{REF} is computed by cubic spline interpolation between integrated spot intensities from 12 reference images interleaved among the 42 time delays (Fig. S6). From a data-collection strategy point of view, this interpolated ratio method is more efficient because it requires fewer total diffraction images in each time series. For this study, the reference images correspond to −1-ns time points, i.e., the X-ray pulse arrives 1 ns in advance of the laser pulse.

Laser-triggered structural changes in the protein crystal cause some reflections to get brighter and some dimmer, with the average ratio for each image expected to be 1. However, the weighted average of all ratios R_{hkl} computed in a single image is generally found to be less than 1 due to laser-induced strain in the crystal, which reduces its diffraction efficiency (Fig. S7). The weights used in the weighted average are derived from the experimental uncertainty of R_{hkl} according to $w = 1/\sigma_R^2$; before processing the data further, they are put on a common scale by rescaling the ratios so the weighted average for each time point is 1.

Excitation Degree Scaling. If an R_{hkl} is sensitive to laser-induced structural changes, it will deviate from unity by a factor that is proportional to the excitation degree, which can vary due to differences in the laser pump fluence. The R_{hkl} can be corrected for differences in the excitation degree by a simple scaling procedure using

$$R^s_{hkl} = 1 + s_i(R_{hkl} - 1)$$

where s_i is the scale factor corresponding to time series i. We find the set of s_i that minimizes the differences between redundant R^s_{hkl} acquired at different orientations and with different crystals.

Outlier Rejection. Provided the crystal orientation remains stable through the time series, the time dependence of R_{hkl} is expected to evolve smoothly and monotonically. However, laser excitation launches an acoustic shock wave in the protein crystal, and occasionally causes the crystal to slip or twitch in the capillary, an event that generates a discontinuity in R_{hkl}. Time series that suffer from sudden changes in crystal orientation are excluded from the merging step.

R_{hkl} Merging. Instead of merging intensities time-point by time-point, we merge complete R^s_{hkl} time series with the weight for each series computed from the average uncertainty across the series, i.e., $w = 1/\sigma_R^2$. If the crystal orientation slips during acquisition of a time series, that time series is rejected. This vector-based approach to merging ensures that the completeness and weights used to calculate the electron density maps are the same throughout each time series, thereby improving the accuracy of our electron density maps and our refined kinetic rate constants.

Time-Dependent Electron Density Map Generation. The merged R^s_{hkl} vectors characterize the time-dependent change in scattering power for each observed reflection. The R^s_{hkl} are converted to structure factor amplitude differences using ground-state structure factor amplitudes calculated from a high-resolution (1.25 Å) room-temperature structure of WT photoactive yellow protein (PYP) acquired under similar conditions (PDB ID code 2ZOH). This high-resolution structure is also used to phase the experimental time-dependent structure factor amplitudes, whose Fourier transform produced the electron density maps used to generate Movie S2 and the 100-ps time-resolved snapshots shown in Fig. 3.

Real-Space Global Analysis Method. The time-resolved electron-density difference maps used to produce each frame in Movie S2 have contributions from one or more intermediates. To extract electron-density difference maps for the intermediates represented in the experimental data and determine the kinetics for their interconversion, we developed a real-space global analysis approach in which the kinetic rate parameters used to define the time-dependent populations of putative intermediates are refined by nonlinear least squares, whereas the electron-density difference maps for the corresponding intermediates are determined by linear least squares. We start with a plausible kinetic model (Fig. 1*C*) whose corresponding rate equations account not only for the first-order processes for structure interconversion, but also for the rate of photoactivation, which depends on the instrument response function, i.e., the convolution of the laser and X-ray pulses. The ability to properly account for the experimental instrument response function is crucial for accurate determination of lifetimes approaching its width, which in this case is ∼150 ps.

We recover "base" electron-density difference maps for the intermediates, $\Delta\boldsymbol{\rho}_b$, by finding the least-squares solution to

$$\Delta\boldsymbol{\rho}_t \cong \mathbf{P}_t \Delta\boldsymbol{\rho}_b,$$

where $\Delta\boldsymbol{\rho}_t$ is a $42 \times n$ matrix representing 42 observed time-resolved electron-density difference maps, $\mathbf{P}_t$ is a 42×4 matrix representing the time-dependent populations for each of four intermediates in our kinetic model (Fig. 4*B*), and $\Delta\boldsymbol{\rho}_b$ is a $4 \times n$ matrix representing four base electron-density difference maps, one for each intermediate. The parameters in our kinetic model are refined iteratively using the Marquardt–Levenberg algorithm, which minimizes the residual found when solving this linear equation. Because structural changes are largest in the vicinity of the *p*-coumaric acid (pCA) chromophore, the least-squares refinement was confined to n = 4,983 voxels found within 2.5 Å of the chromophore. This restricted-range approach enhances the sensitivity of the kinetic model to structural dynamics occurring in the chromophore region, and improves the accuracy of its refined parameters. Once the population matrix is known, we solve this linear equation using all voxels in the unit cell (n = 2,689,600) and generate complete base maps.

Note that this global analysis method could have been applied to structure factors in reciprocal space rather than electron density voxels in real space. However, it is not possible to define a region of interest in reciprocal space, so the accuracy of the refined kinetic rate parameters would be poorer than can be achieved with our real-space approach.

Not all parameters in our kinetic model are refinable by least-squares methods and must be specified independently. For example, the photoproduct yield affects the initial pR_0 population, and incorrect assumptions about this yield lead to contamination of its base map with electron density from the ground state. This contamination was found to be negligible when the photoproduct yield was set to 10%. When the photoproduct yield of pB_0 was assumed to be 10% as well, the electron density map assigned to pB_0 appeared to be a 50:50 mixture of the ground and pB_0 states (Fig. S8*A*); when set to 5%, the electron density map for pB_0 is well described by a single structure (Fig. S8*B*). Hence, ~50% of the pR_2 population short-circuits to the ground state during the pR_2-to-pB_0 transition, and our kinetic model was modified accordingly.

Although our real-space global analysis approach recovers electron density maps for all intermediates in the model, the maps generated are not guaranteed to be chemically sensible. Therefore, structure refinement is required to assess and validate the proposed model.

Structure Refinement. Atomic structures for each intermediate in the model were refined in reciprocal space using phenix.refine, a program that implements the restrained maximum-likelihood method (3). This program requires as input structure factor amplitudes and their estimated uncertainties. To generate $\Delta\mathbf{F}_b$, the base structure factor amplitude differences, we Fourier-transformed $\Delta\boldsymbol{\rho}_b$, the complete base difference density maps generated by our global analysis. To generate $\boldsymbol{\sigma}^2(\Delta F_b)$, the variance for the base structure factor amplitude differences, we used linear algebra to propagate the experimental variances for $\boldsymbol{\sigma}^2(\Delta F_t)$, which are derived from photon-counting statistics.

To mitigate the effects of modeling error, we used the method of difference refinement (4), using as input for the refinement program the calculated ground-state structure factors, $\mathbf{F}_c$, plus our structure factor amplitude differences, $\Delta\mathbf{F}_b$ (intermediate minus ground state):

$$\mathbf{F}_b = \mathbf{F}_c + \Delta\mathbf{F}_b.$$

The restraints needed for the pCA chromophore are not included in the restraints library of the PHENIX package, and were instead generated by the program eLBOW (Electronic Ligand Bond Builder and Optimization Workbench), a utility distributed with PHENIX. The eLBOW-generated restraints were used with one exception: the pCA dihedral bond angle restraints were set to 0/180 ± 4°, as opposed to eLBOW default values of 0/180 ± 30°. The default variance proved far too generous, and allowed the default bond angle restraints (120 ± 3°) to dictate the structure. Indeed, the default restraints produced a structure in which the ~90° twist between the phenolate and the carbonyl was absorbed almost entirely by the C1′–C3 = C2–C1 dihedral angle, in stark contrast to DFT calculations, which distribute the twist among all three dihedral angles between the phenolate and the carbonyl. For our refinement, the three dihedral bond angles were assigned the same restraints, a choice justified by the fact that the pCA absorbance is red-shifted in the pR_0 state, and must therefore remain well-conjugated.

The crystallographic data and data collection statistics are summarized in Table S2, and the refinement statistics are summarized in Table S3. The signal-to-noise ratio (S/N) of the electron density maps for each intermediate reflects the number of images in which the intermediate is represented, as well as its relative population. Because the photoproduct yield is ~10%, the S/N of the intermediates is ~10-fold poorer than that for the ground state. However, these intermediates are represented in numerous frames of the time series, which improves their S/N. Note that the S/N for pR_0 is poorer than that for pR_1 and pR_2, reflecting the smaller number of frames in which this intermediate is represented.

Kinetic Model Validation. The validity of a kinetic model can be assessed by comparing the experimental electron density maps with those computed from the refined atomic coordinates for each intermediate. If differences between the experimental and computed electron density maps rise above the noise and vary systematically in space, the kinetic model is deemed invalid and needs to be modified accordingly. The aim is to find a kinetic model that accounts for the time-resolved electron density maps with the fewest possible intermediates and rate parameters, i.e., Occam's razor. The fit residuals visualized in Fig. S2 demonstrate that the kinetic model used in this study reproduces the experimentally determined time-resolved structures with high fidelity. This validation test failed for the first kinetic model tried: when the pR_0-to-pR_1 transition was considered irreversible, the residuals between the calculated and experimental electron densities for pR_1 revealed significant contamination by pR_0 (Fig. S9). After making the pR_0-to-pR_1 transition reversible, this contamination disappeared (Fig. S10).

Density Functional Theory Calculations. The molecular structures of all experimentally observed states (pG, pR_0, pR_1, pR_2, and pB_0) were optimized using dispersion-corrected density functional theory, D-BP86 (5–8), with the Karlsruhe split valence polarized basis set, def2-SVP (9). Using starting coordinates from the X-ray–refined structures of pR_0, pR_1, and pR_2, density functional theory (DFT) optimization of the pCA chromophore in vacuum converged to the same *cis* state. Clearly, interactions with the protein are required to stabilize the intermediates observed in PYP. The protein cavity in which pCA resides is surrounded by 12 residues (Y42, E46, T50, R52, F62, V66, A67, P68, C69, T70, F96, and M100). A quantum chemical model was constructed from pCA and these residues, with Tyr42, Glu46, and Arg52 protonated. The pCA was deprotonated in all states except pB_0 (see below). To trim the size of the model, residues whose backbone atoms are not involved in hydrogen bonding networks were terminated at the Cβ position. This protein model, which is comprised of 176 atoms (192 atoms in pB_0), was optimized with the backbone atoms constrained to their X-ray–refined coordinates. All DFT structures were found to be in excellent agreement with the X-ray structures (Fig. S4), suggesting that the protonation-state assignments are correct. Indeed, protonation of pCA in the pR states, or deprotonation of pCA in the pB_0 state, led to large discrepancies between the X-ray and DFT structures.

DFT calculations were also carried out to evaluate the relative quantum chemical energies for each pR state, relevant hydrogen bond energies, as well as chromophore strain energy. The chromophore strain energy was calculated as the difference between the energy of the chromophore in its protein- and vacuum-relaxed conformations. For these single-point energy calculations, we used Becke's three-parameter functional with empirical dispersion correction, D-B3LYP (7, 8, 10, 11) and a triple-ζ basis set augmented with polarization functions, def2-TZVP (12). Solvation effects were modeled using COSMO (13) with the dielectric constant set to 4. All quantum chemical calculations were performed using TURBOMOLE version 6.3 (14).

1. Coppens P, et al. (2009) The RATIO method for time-resolved Laue crystallography. *J Synchrotron Radiat* 16(Pt 2):226–230.
2. Vorontsov I, Pillet S, Kaminski R, Schmokel MS, Coppens P (2010) LASER—a program for response-ratio refinement of time-resolved diffraction data. *J Appl Cryst* 43:1129–1130.
3. Adams PD, et al. (2010) PHENIX: A comprehensive Python-based system for macromolecular structure solution. *Acta Crystallogr D Biol Crystallogr* 66(Pt 2):213–221.
4. Terwilliger TC, Berendzen J (1996) Bayesian difference refinement. *Acta Crystallogr D Biol Crystallogr* 52(Pt 5):1004–1011.
5. Vosko SH, Wilk L, Nusair M (1980) Accurate spin-dependent electron liquid correlation energies for local spin-density calculations: A critical analysis. *Can J Phys* 58(8): 1200–1211.
6. Perdew JP (1986) Density-functional approximation for the correlation energy of the inhomogeneous electron gas. *Phys Rev B Condens Matter* 33(12):8822–8824.
7. Becke AD (1988) Density-functional exchange-energy approximation with correct asymptotic behavior. *Phys Rev A* 38(6):3098–3100.
8. Grimme S (2006) Semiempirical GGA-type density functional constructed with a long-range dispersion correction. *J Comput Chem* 27(15):1787–1799.
9. Schafer A, Horn H, Ahlrichs R (1992) Fully optimized contracted Gaussian-basis sets for atoms Li to Kr. *J Chem Phys* 97(4):2571–2577.
10. Lee CT, Yang WT, Parr RG (1988) Development of the Colle-Salvetti correlation-energy formula into a functional of the electron density. *Phys Rev B Condens Matter* 37(2):785–789.
11. Becke AD (1993) Density-functional thermochemistry. 3. The role of exact exchange. *J Chem Phys* 98(7):5648–5652.
12. Weigend F, Ahlrichs R (2005) Balanced basis sets of split valence, triple zeta valence and quadruple zeta valence quality for H to Rn: Design and assessment of accuracy. *Phys Chem Chem Phys* 7(18):3297–3305.
13. Klamt A, Schuurmann G (1993) Cosmo: A new approach to dielectric screening in solvents with explicit expressions for the screening energy and its gradient. *J Chem Soc Perk T* 2(5):799–805.
14. Ahlrichs R, Bar M, Haser M, Horn H, Kolmel C (1989) Electronic-structure calculations on workstation computers: The program system TURBOMOLE. *Chem Phys Lett* 162(3): 165–169.

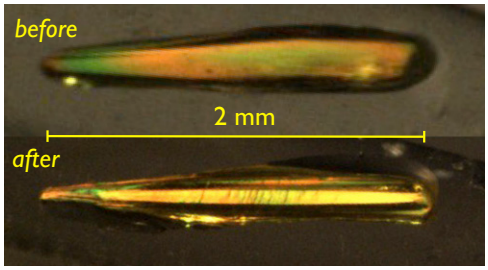

Fig. S1. Before and after photos of PYP7, one of nine crystals used to acquire time-resolved diffraction data. The crystal was viewed through crossed polarizers to suppress the background; variations in color are not real, but arise due to crystal birefringence. The "before" image appears homogeneous across its length. The image acquired after X-ray exposure reveals radiation-induced cracking of the crystal. These small cracks increase crystal mosaicity and reduce the diffraction quality. A total of 336 images were acquired from this crystal, i.e., 6 orientations with 56 time-resolved images acquired per orientation (including 12 interleaved −1-ns reference images).

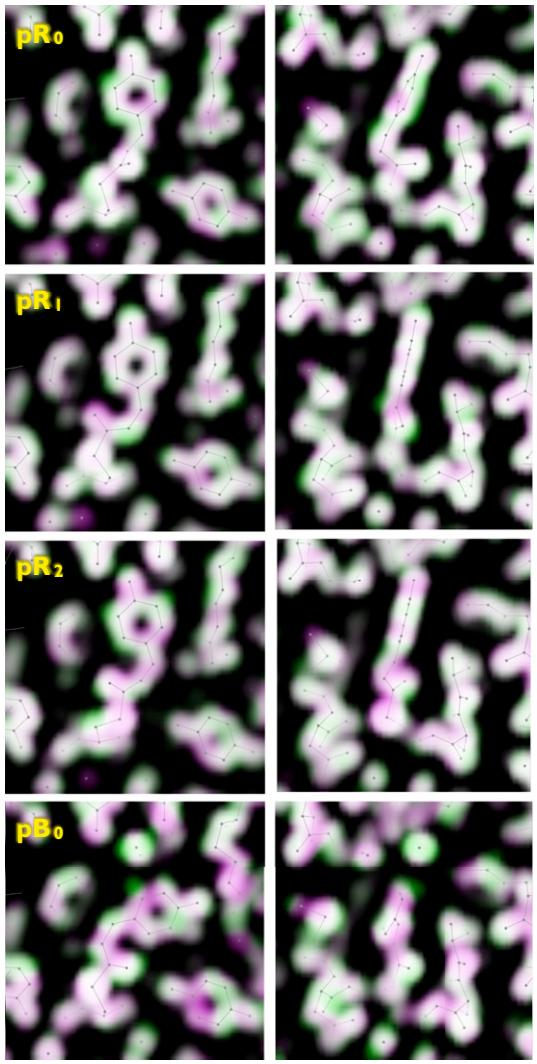

Fig. S2. Fit residuals are visualized via color-coded overlays of experimental (green) and calculated (magenta) electron density maps for pR_0, pR_1, pR_2, and pB_0 intermediates. The experimental maps were obtained by global analysis of the time-resolved structure-factor amplitudes. The calculated maps were generated from single structures refined against the experimental maps. The pastel coloration of the pCA electron density appears to vary randomly, demonstrating that the sequential kinetic model in Fig. 4*A* accounts for the time-dependent electron density changes with high fidelity.

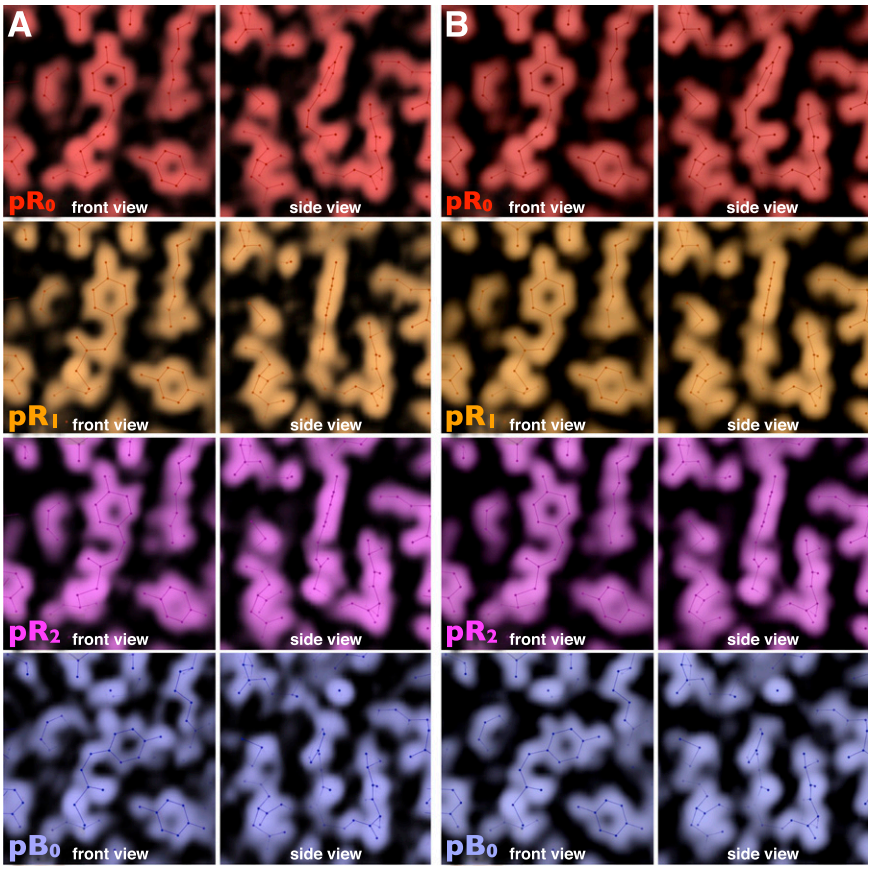

Fig. S3. Electron density maps of photocycle intermediates obtained by global analysis. (*A*) Calculated using phases from the ground state (pG) model for each of the four intermediates. (*B*) Calculated using refined phases from the model of each intermediate (same as in Fig. 4).

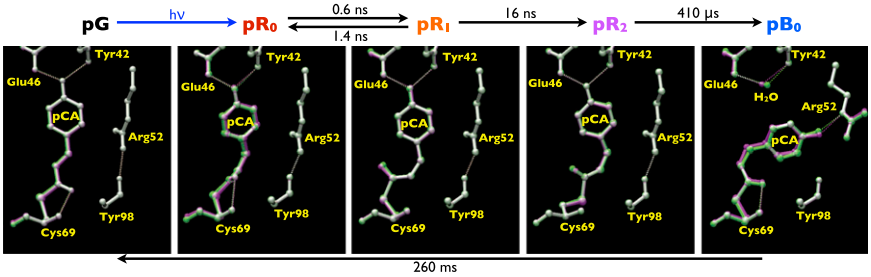

Fig. S4. Comparison of X-ray–refined (green) and DFT–optimized (magenta) structures. Where the structures overlap, they blend to white. For clarity, only the pCA and its hydrogen bonding partners are shown.

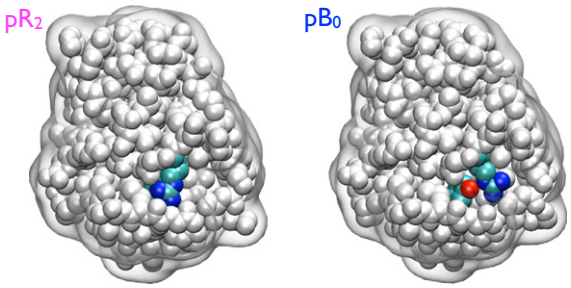

Fig. S5. During the pR_2-to-pB_0 transition, Arg52 swings from a closed to an open conformation, exposing the phenolate oxygen (red sphere) to water. This open conformation facilitates penetration of a water molecule into the pCA cavity, which is stabilized by hydrogen bonds with Tyr42 and Glu46, and likely prolongs the lifetime of the pB_0 state (rendered with VMD).

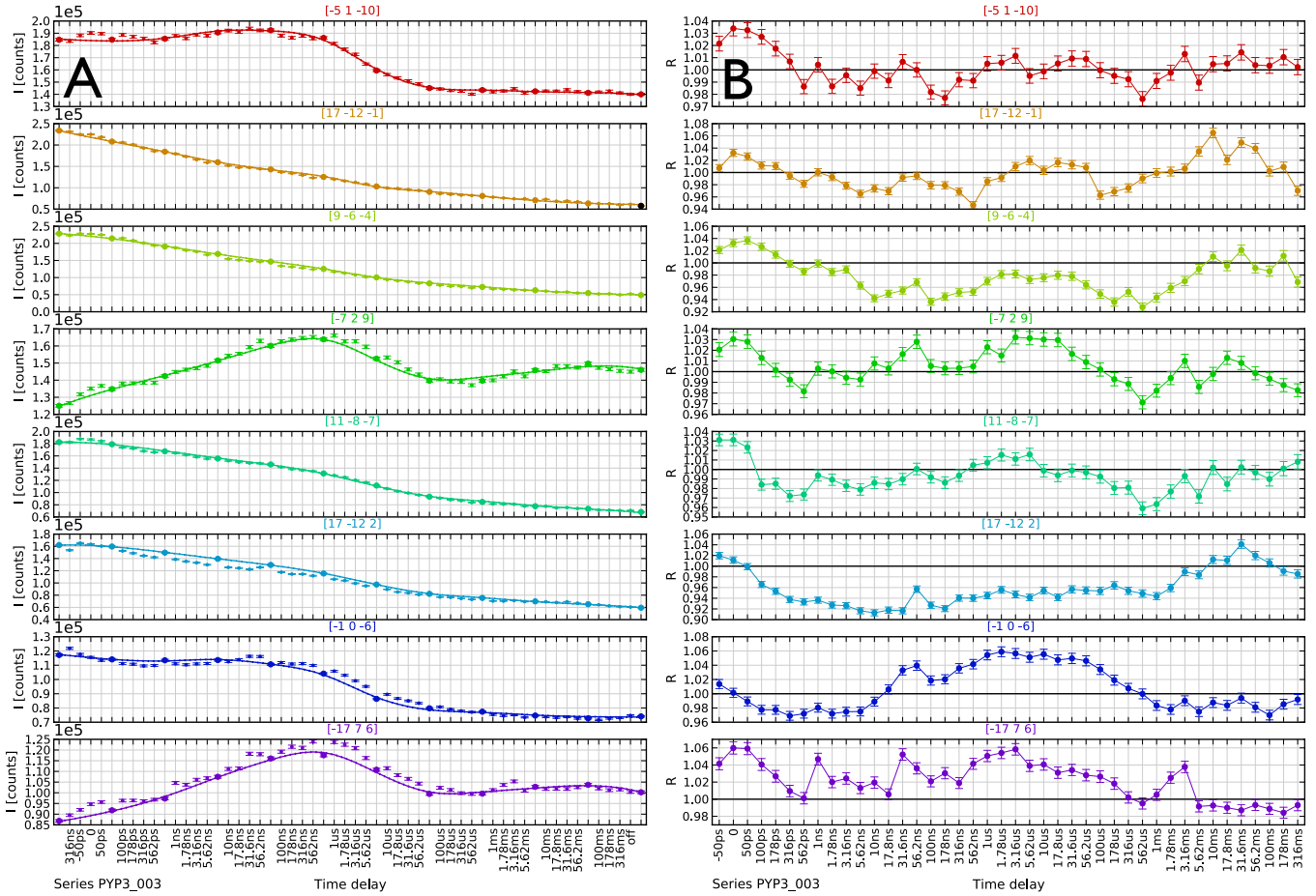

Fig. S6. Interpolated ratio method. (*A*) A cubic spline (solid line) interpolates between the integrated spot intensities in the reference images (−1-ns time points; large filled circles). The interpolated intensities are used to compute ratios, $R_{hkl} = I_t/I_{-1ns}$. The subset of reflections shown corresponds to the strongest indexed reflections found at a particular crystal orientation. Their integrated intensities (photons) have been normalized against I0, the relative X-ray intensity. The variation in intensity across the time series is due in part to crystal morphology, which leads to changes in the diffracting volume as the crystal is translated from one end to the other. (*B*) Time dependence of ratios calculated from data in *A*. Time-dependent changes in the protein structure cause some reflections to get brighter, and some dimmer.

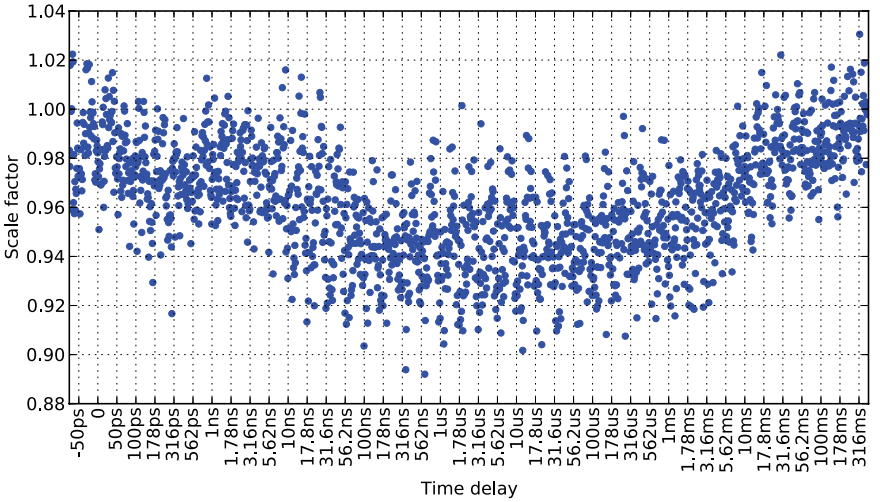

Fig. S7. Weighted average of R_{hkl} as a function of time delay for all 41 time series used in our structure analysis.

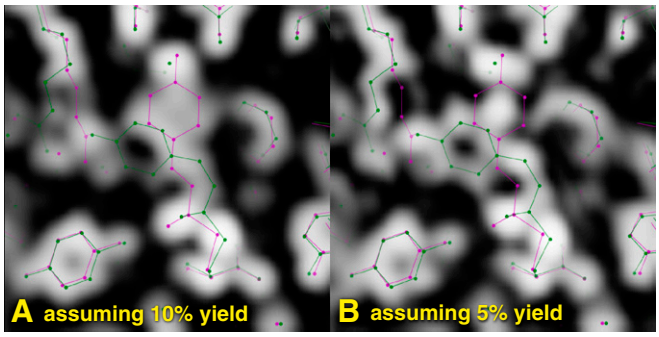

Fig. S8. Time-resolved electron density maps acquired 1 ms after photoexcitation (2 mF_O – DF_C; phased with ground-state model). The two maps were extrapolated to 100% population assuming a photoproduct yield of 10% (*A*) and 5% (*B*). Superimposed are ball-and-stick models of the pG ground state (magenta) and pB_0 state (green).

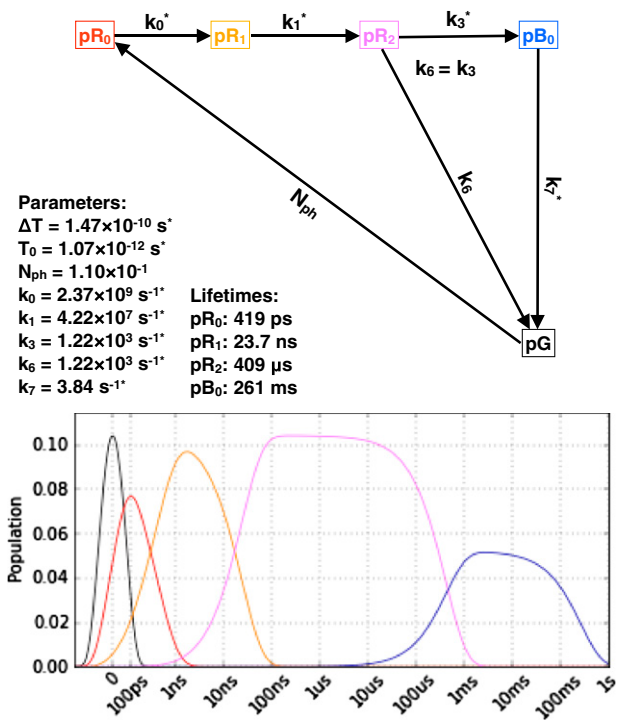

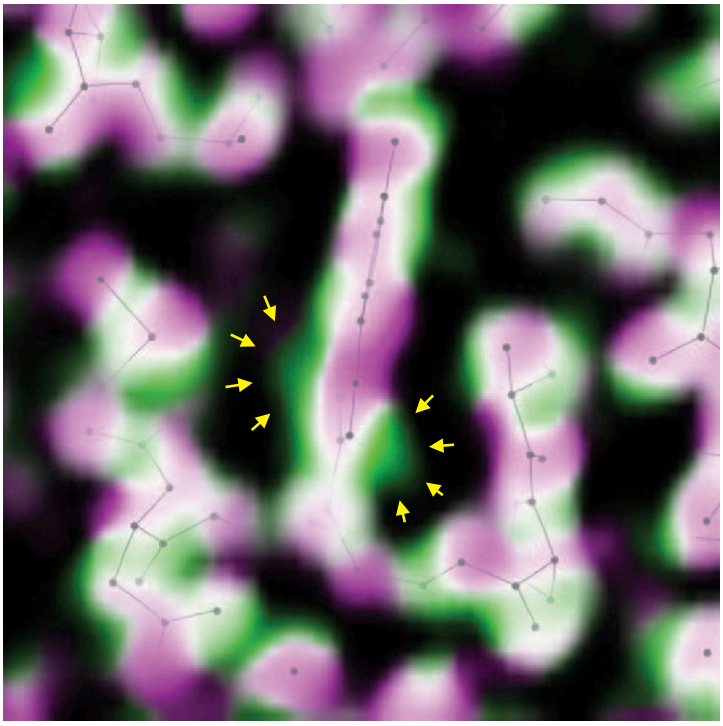

Fig. S9. (*Left*) Sequential kinetic model; refined parameters; and the corresponding population dynamics. (*Right*) Color-coded overlay of the pR_1 intermediate: atomic model density (magenta; F_O map phased with pR_1 model) and global analysis density (green; 2 mF_O – DF_C map phased with pR_1 model); ball-and-stick model of pR_1 state (gray). The excess green density highlighted by yellow arrows is found in the same location as the carbonyl oxygen in the pR_0 state, suggesting persistence of that state.

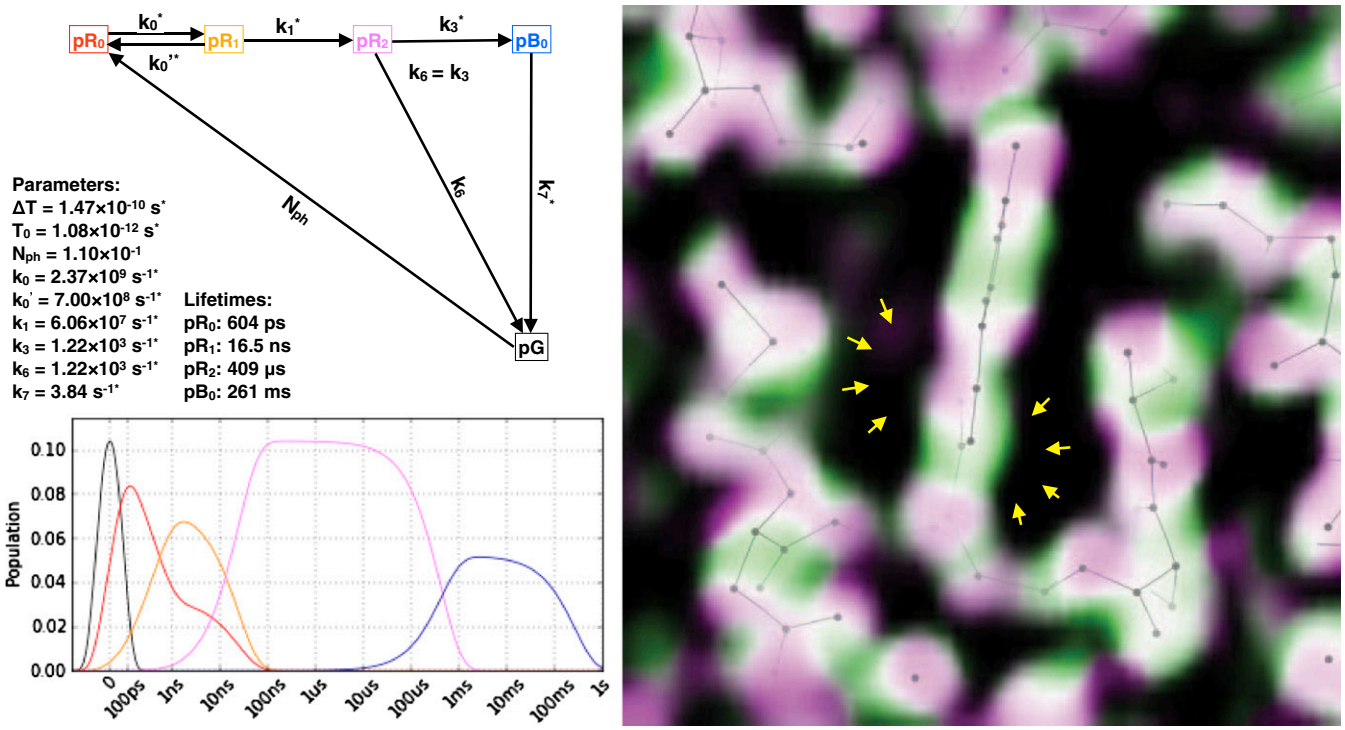

Fig. S10. (*Left*) Nonsequential kinetic model with equilibrium between pR_0 and pR_1; refined parameters; and the corresponding population dynamics. (*Right*) Color-coded overlay of the pR_1 intermediate: atomic model density (magenta; F_O map phased with pR_1 model) and global analysis density (green; 2 $mF_O - DF_C$ map phased with pR_1 model); ball-and-stick model of pR_1 state (gray). The electron density differences are modest, with little evidence for pR_0 contamination.

Table S1. Properties of each intermediate in the PYP photocycle

	pR_0	pR_1	pR_2	pB_0	pG
Lifetimes	600 ps	16 ns	410 us	260 ms	—
Stereochemistry					
Phe–C3=C2	27°	5°	16°	29°	7°
C1′–C3=C2–C1	*cis* (31°)	*cis* (–8°)	*cis* (2°)	*cis* (–1°)	*trans* (169°)
C3=C2–C1–S	*anti A*– (–152°)	*anti T* (174°)	*anti T* (175°)	*anti T* (155°)	*anti T* (169°)
C2–C1–S–Cβ	*anti A*– (–124°)	*syn C* (–24°)	*anti T* (–168°)	*anti T* (171°)	*anti T* (179°)
C1–S–Cβ–Cα	*syn G*– (–80°)	*syn G*- (–87°)	*anti A*+ (104°)	*syn G*– (–72°)	*syn G*- (–81°)
Hydrogen bonds					
pCA···Tyr42	2.54	2.57	2.47	—	2.51
pCA···Glu46	2.75	2.64	2.61	—	2.58
pCA···Cys69	3.04	—	—	2.91	2.82
pCA···Arg52	—	—	—	2.92	—
Cα··Cα distances					
Cys69–Tyr42	17.31	17.29	17.23	17.81	17.82
Cys69–Glu46	15.28	15.39	15.29	15.57	16.04
Cys69–Arg52	14.29	14.3	14.29	14.34	14.72
pCA S-O4 distance	8.30	8.62	8.67	8.28	9.05
DFT energies					
Total (relative to pG)	22.8	23.9	16.8	*	0
pCA···Tyr42	11.9	12.9	11.7	—	11.3
pCA···Glu46	8.3	9.5	10.2	—	10.9
pCA···Cys69	8.4	—	—	10.4	9.0
pCA···Arg52	—	—	—	10.7	—
pCA strain	16.1	10.6	6.2	5.7	4.9

Stereochemistry designations follow IUPAC convention. Hydrogen bond distances and other distances are given in Å. DFT energies are given in kcal·mol^{-1}. The pCA strain energy corresponds to the chromophore only. The shaded cells highlight configurations/distances that deviate significantly from pG.

*The energy of the pB_0 intermediate is not estimated because the particle number in its quantum chemical model is not conserved relative to pG.

Table S2. Crystallographic data and data collection statistics for the 41 time series used in our data analysis

Space group	P63
Unit cell a, b, c, Å	66.833, 66.833, 40.947
α, β, γ,°	90, 90, 120
Resolution, Å	13.3–1.60
Reflections (observed)	10,605
13.28–2.93 Å	1,756
2.93–2.32 Å	2,062
2.32–2.02 Å	2,078
2.02–1.84 Å	1,888
1.84–1.70 Å	1,675
1.70–1.60 Å	1,146
Reflections ($I/\sigma > 2$)	10,544
13.28–2.93 Å	1,753
2.93–2.32 Å	2,055
2.32–2.02 Å	2,072
2.02–1.84 Å	1,876
1.84–1.70 Å	1,662
1.70–1.60 Å	1,126
Completeness (observed)	0.76
13.28–2.93 Å	0.76
2.93–2.32 Å	0.89
2.32–2.02 Å	0.90
2.02–1.84 Å	0.81
1.84–1.70 Å	0.72
1.70–1.60 Å	0.49
Completeness ($I/\sigma > 2$)	0.76
13.28–2.93 Å	0.76
2.93–2.32 Å	0.89
2.32–2.02 Å	0.89
2.02–1.84 Å	0.81
1.84–1.70 Å	0.72
1.70–1.60 Å	0.49
Redundancy	5.11
13.28–2.93 Å	4.56
2.93–2.32 Å	6.09
2.32–2.02 Å	6.06
2.02–1.84 Å	5.69
1.84–1.70 Å	4.40
1.70–1.60 Å	2.56
$\langle I/\sigma_I \rangle$	34.5
13.28–2.93 Å	64.5
2.93–2.32 Å	57.2
2.32–2.02 Å	41.5
2.02–1.84 Å	25.2
1.84–1.70 Å	13.2
1.70–1.60 Å	5.4
R_{sym}	0.20
13.28–2.93 Å	0.12
2.93–2.32 Å	0.25
2.32–2.02 Å	0.22
2.02–1.84 Å	0.23
1.84–1.70 Å	0.21
1.70–1.60 Å	0.15

The structure factors observed are in common for all 42 time delays in each series (−50 ps, 0, 50 ps, +100 ps to 316 ms with four steps per decade). The signal-to-noise ratio does not change significantly across the time delays.

Table S3. Refinement statistics for each intermediate in the PYP photocycle

Intermediate	pR_0	pR_1	pR_2	pB_0
PDB ID code	4B9O	4BBT	4BBU	4BBV
R_{work}	0.221	0.169	0.165	0.255
R_{free}	0.308	0.228	0.218	0.360
No. of atoms	1,126	1,126	1,126	1,127
Protein	976	976	976	976
Water	139	139	139	140
Chromophore	11	11	11	11
B-factors, A^2	20.3	23.1	26.2	22.7
Protein, A^2	19	21.3	24.4	21.7
Water, A^2	30.2	36.2	39.2	30.2
Chromophore, A^2	11.1	15.7	19.6	15.8
Reflections ($I/\sigma_I > 2$)	7,038	8,171	8,940	6,948
13.28–2.93 Å	1,657	1,707	1,738	1,633
2.93–2.32 Å	1,724	1,877	1,962	1,699
2.32–2.02 Å	1,544	1,779	1,904	1,514
2.02–1.84 Å	1,151	1,405	1,579	1,108
1.84–1.70 Å	688	969	1,164	704
1.70–1.60 Å	274	434	593	290
Completeness ($I/\sigma_I > 2$)	0.51	0.59	0.64	0.50
13.28–2.93 Å	0.71	0.74	0.75	0.70
2.93–2.32 Å	0.74	0.81	0.85	0.73
2.32–2.02 Å	0.67	0.77	0.82	0.65
2.02–1.84 Å	0.50	0.61	0.68	0.48
1.84–1.70 Å	0.30	0.42	0.50	0.30
1.70–1.60 Å	0.12	0.19	0.26	0.13
$\langle I/\sigma_I \rangle$	4.6	6.9	11.6	5.1
13.28–2.93 Å	11.0	16.9	30.1	13.3
2.93–2.32 Å	6.9	10.6	17.7	7.7
2.32–2.02 Å	4.7	7.2	11.4	5.0
2.02–1.84 Å	2.7	4.0	6.1	2.7
1.84–1.70 Å	1.4	2.1	2.9	1.4
1.70–1.60 Å	0.7	0.9	1.2	0.6

The signal-to-noise ratio depends on the number of time points in which the intermediate is observed, and the yield with which it is generated.

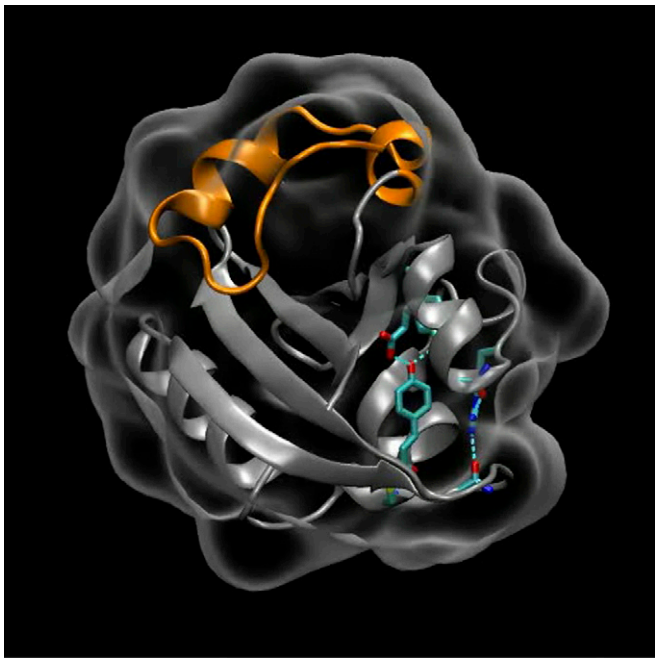

Movie S1. Ground-state structure of PYP. The backbone is rendered in ribbon with the N-terminal domain colored orange. The atoms rendered in licorice are colored according to type: C (cyan); N (blue); O (red); S (yellow). Relevant hydrogen bonds are indicated as dashed cyan lines (rendered with VMD).

Movie S1

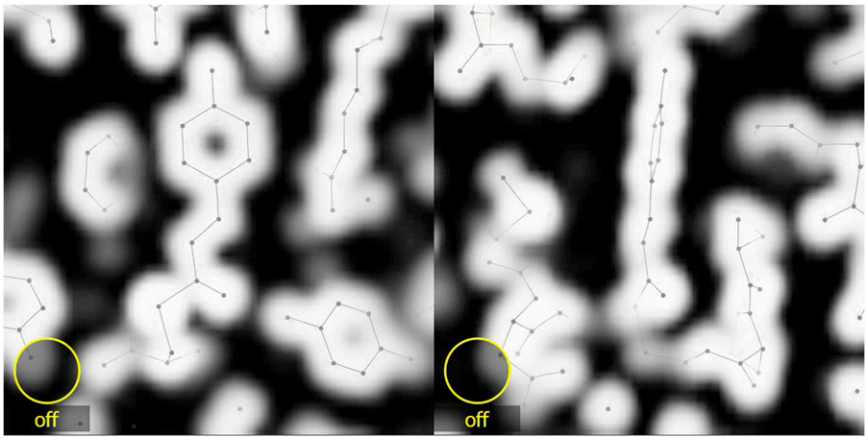

Movie S2. Time-dependent electron density maps spanning 10 decades of time. Both frontal and side views are shown. The ground state electron density maps are colored magenta, and the time-resolved maps are colored green. Where magenta and green overlap, the electron density blends to white. The magenta-to-green color gradient unveils the direction of atomic motion.

Movie S2

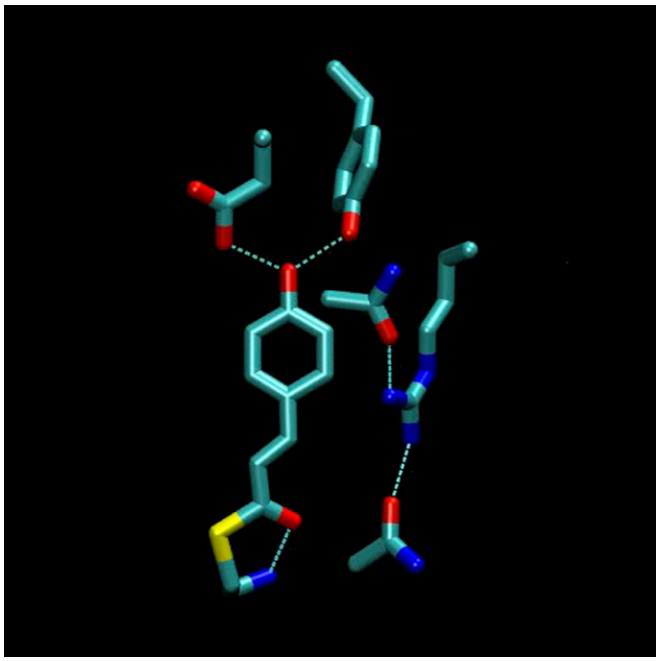

Movie S3. Color-coded rotating overlay of pCA structures and relevant side chains: pG (cyan); pR_0 (red); pR_1 (orange); pR_2 (magenta); and pB_0 (blue). After the first revolution, which shows pG only, overlaid structures before and after each successive transition are shown. This approach highlights the structural changes occurring during each transition. Water molecules are rendered as red spheres. Hydrogen bonds are rendered as dashed cyan lines (rendered with VMD).

Movie S3

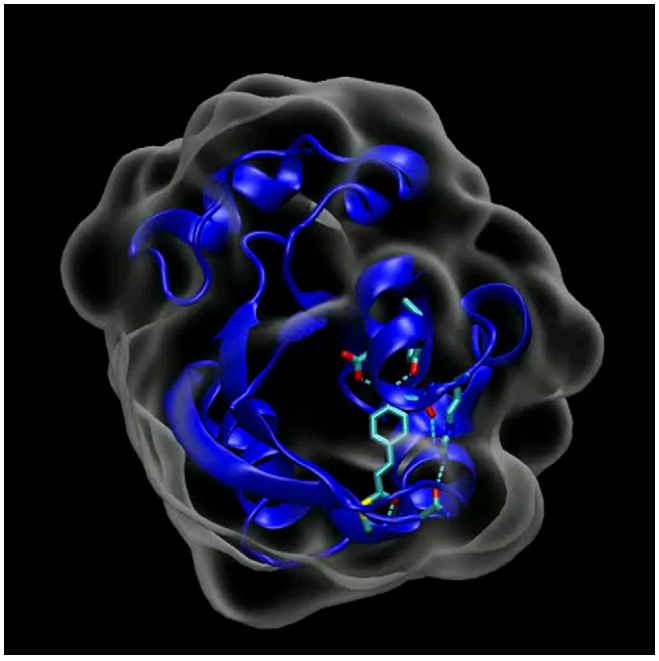

Movie S4. Color-coded structures of pG, pR_0, pR_1, pR_2, and pB_0, as in Fig. 4. The pCA and relevant side chains are colored cyan (pG), red (pR_0), orange (pR_1), magenta (pR_2), and blue (pB_0). Hydrogen bonds discussed in the main text are indicated as dashed cyan lines. The backbone is rendered blue-white-red according to atomic displacement relative to the pG state, with red in the color scale corresponding to 0.5 Å. The intermediate structure shown advances after each period in a rock-and-roll motion (rendered with VMD).

Movie S4